nature materials

Article

https://doi.org/10.1038/s41563-022-01386-z

Crossover from Ising- to Rashba-type superconductivity in epitaxial Bi_2Se_3/monolayer $NbSe_2$ heterostructures

In the format provided by the authors and unedited

Content:

I. Supplementary Text for Extended Data Figs. 1 to 10

Extended Data Fig. 1 shows the reflection high energy electron diffraction (RHEED) patterns of the bilayer graphene terminated 6H-SiC (0001) substrate, the monolayer $NbSe_2$ film, and the 5 QL Bi_2Se_3/monolayer $NbSe_2$ heterostructure. The sharp RHEED patterns of the monolayer $NbSe_2$ film (Extended Data Fig. 1b) and the 5 QL Bi_2Se_3/monolayer $NbSe_2$ heterostructure (Extended Data Fig. 1c) indicate the highly ordered crystallinity of our Bi_2Se_3/monolayer $NbSe_2$ heterostructures.

Extended Data Figs. 2a to 2c show the cross-sectional annular dark-field scanning transmission electron microscope (ADF-STEM) images of the 6QL Bi_2Se_3/monolayer $NbSe_2$ heterostructure along different orientations. As described in the main text, we observed a BiSe bilayer with a cubic lattice structure at the Bi_2Se_3/$NbSe_2$ interface, which reduces the large lattice mismatch between monolayer $NbSe_2$ and Bi_2Se_3 layer (~20%)[1]. Moreover, our ADF-STEM measurements show that the atomic structures of the monolayer $NbSe_2$ and Bi_2Se_3 layers can not be simultaneously resolved, which indicates that a misorientation exists between the monolayer $NbSe_2$ and Bi_2Se_3 layers. The corresponding energy dispersive spectroscopy (EDS) maps of Si, Nb, Bi, and Se further confirm the high quality of our Bi_2Se_3/monolayer $NbSe_2$ heterostructures (Extended Data Figs. 2d and 2e).

Extended Data Figs. 3a and 3b show the Fermi surface maps of monolayer $NbSe_2$ and the 1QL Bi_2Se_3/monolayer $NbSe_2$ heterostructure. For monolayer $NbSe_2$, we observed a hole pocket near the Γ point and a hole pocket near the K point of the Brillouin zone (BZ) (Extended Data Fig. 3a). After the deposition of 1QL Bi_2Se_3, one more electron pocket with a circular shape from 1QL Bi_2Se_3 appears near the Γ point, suggesting its isotropic property (Extended Data Fig. 3b).

Next, we studied the electronic band alignment between monolayer $NbSe_2$ and the 1QL Bi_2Se_3/monolayer $NbSe_2$ heterostructure. For monolayer $NbSe_2$, a hole pocket crosses the chemical potential near the Γ point, confirming its monolayer characteristic (Extended Data Fig. 3c)[2,3]. For the 1QL Bi_2Se_3/monolayer $NbSe_2$ heterostructure, a near-parabolic band appears near the Γ point (Extended Data Fig. 3d), which is analogous to that of the 1QL Bi_2Se_3 directly grown on epitaxial bilayer graphene substrates[4]. In addition to this electron pocket of 1QL Bi_2Se_3, the valence bands of monolayer $NbSe_2$ can still be resolved but with a weaker band spectrum intensity (Extended Data Fig. 3d). To quantitively study the band alignment, we extracted the energy distribution curves (EDCs) at the Γ point in both monolayer $NbSe_2$ and the 1QL Bi_2Se_3/monolayer $NbSe_2$ heterostructure (Extended Data Fig. 3e). We found that the peak positions of one specific valence band of monolayer $NbSe_2$ remain the same before and after the deposition of 1QL Bi_2Se_3. This observation implies an ignorable charge transfer between monolayer $NbSe_2$ and Bi_2Se_3 layers in our Bi_2Se_3/monolayer $NbSe_2$ heterostructures.

To highlight the Rashba-type bulk quantum well (QW) bands and spin-nondegenerate Dirac surface states (SSs), we performed the second derivative analysis of the ARPES data in Figs. 2b to 2f of the main text. For the m=2 sample, besides the band bending-induced Rashba-type SSs (Ref. [4]), a bulk QW state with large Rashba band splitting (i.e. QW1) appears (Extended Data Fig. 4a). For the $m \geq 3$ samples, the SSs become gapless, a signature of crossover from 2D to 3D TI

regimes[5]. We observed one more Rashba-type bulk QW state (i.e. QW2) (Extended Data Figs. 4b to 4e). In addition to the method used in the manuscript to estimate the Rashba coupling strength α_R, we can also deduce α_R by fitting the spin-split Rashba band dispersions using the following equation[6]:

$$E(k) = E_0 + \frac{\hbar^2 k^2}{2m^*} \pm (\alpha_R k + \beta_R k^3) \quad \text{(S1)}$$

Here m^* is the effective electron mass and β_R is the 3rd order Rashba splitting parameter. Since the inner and outer branches of the Rashba bands in Bi_2Se_3/monolayer $NbSe_2$ heterostructures merge at finite k rather than the time-reversal invariant momenta at Brillouin zone centers and/or boundaries, we introduced an isotropic 3rd order Rashba term in Eq. (S1).

Through the fitting process for the ARPES data, we obtained the 1st order Rashba splitting parameter α_R~0.95 eV·Å for the $m = 2$ sample, which is in good agreement with α_R~1.0 eV·Å calculated by $2E_R/k_R$. We noted that the value of α_R in the 2QL Bi_2Se_3/monolayer $NbSe_2$ heterostructure is comparable to that of the Rashba splitting of Bi_2Se_3 bulk conduction QW states (α_R~0.79 eV · Å with potassium doping; α_R~1.3 eV · Å with rubidium doping) [7-10] but orders of magnitude larger than that of the Rashba splitting in conventional semiconducting two-dimensional electron gases (α_R~0.09 eV · Å in InAs/GaSb; α_R~0.06 eV · Å in InAs/AlSb; α_R~0.04 eV · Å in InGaAs/InAlAs)[11-13].

Moreover, we found that the α_R value of QW1 decreases with increasing *m* and disappears for the m≥6 samples. However, the α_R value of QW2 decreases slightly with increasing *m* but remains a large value (~0.63 eV·Å) in the *m*=6 sample (Extended Data Fig. 4f). We noted that the α_R value of QW2 is larger than that of QW1 for the $m \geq 5$ samples. This property is different from the band bending induced bulk Rashba-type bands in Bi_2Se_3 single crysltals[7-10].

Next, we discussed the Dirac point (or the middle of the hybridization gap) shift towards bulk conduction bands with increasing *m* (Fig. 2 and Extended Data Fig. 4). This phenomenon has been observed in MBE-grown Bi_2Se_3 films on either metallic or insulating substrates, including bilayer graphene [4], sapphire[14], and Si(111) (Ref. [15]). Therefore, it is unlikely that the charge transfer from the substrates plays a major role in the Dirac point shift in Bi_2Se_3 films with increasing the thickness *m*, as discussed in Ref. [4]. Prior studies have demonstrated that the formation of the Se vacancies is sensitive to the growth conditions [4,16] and the quantum confinement-induced band bending effect in the surface layers of Bi_2Se_3 bulk crystals [10]. Therefore, we speculate that the Dirac point shift in MBE-grown Bi_2Se_3 films might be a result of the film thickness-dependent concentration of Se vacancies or the band bending effect in the surface layers. More experiments are needed to clarify this issue in the future.

Extended Data Figs. 5a and 5b show the *R*-*T* curves of monolayer $NbSe_2$ under different $\mu_0 H_\perp$ and $\mu_0 H_\parallel$. We found that the superconductivity in monolayer $NbSe_2$ is suppressed by an out-of-plane magnetic field much more rapidly than that by an in-plane magnetic field, consistent with prior studies[17,18]. To quantitatively verify the Ising-type superconducting pairing symmetry in our monolayer $NbSe_2$, we plotted its $H_{c2,\perp}$-T and $H_{c2,\parallel}$-T curves. $H_{c2,\perp}$ shows a good linear dependence on *T*, while $H_{c2,\parallel}$ shows a square-root dependence on *T*. The extracted $H_{c2,\parallel}$ at T=0 K is ~25 T, greater than 4.9 times the Pauli limit H_P, ($H_p \sim 1.86 T_c$ ~5.3 T), confirming the Ising-type pairing symmetry in our monolayer $NbSe_2$ (Refs. [17,18]).

Extended Data Fig. 6 shows the magnetoresistance of *m*QL Bi_2Se_3/monolayer $NbSe_2$ heterostructures under in-plane magnetic fields and different temperatures. We normalized the magnetoresistance *R* to the normal resistance at $\mu_0 H_\parallel$ ~6 T for the m=1 sample and $\mu_0 H_\parallel$ ~4 T for the $m \geq 2$ samples, respectively. The $H_{c2,\parallel}$ value is determined as the magnetic field at which the

normalized resistance reaches ~0.5. The $H_{c2,\parallel}$ ~T/T_c phase diagram is shown in Fig. 3b of the main text.

Extended Data Fig. 7 shows the magnetoresistance of monolayer $NbSe_2$ and *m*QL Bi_2Se_3/monolayer $NbSe_2$ heterostructures with *m*=1, 2, and 6 under out-of-plane magnetic fields at different temperatures. We determined the $H_{c2,\perp}$ value as the magnetic field at which the magnetoresistance reaches ~50% of the normal resistance. The $H_{c2,\perp}$ ~T/T_c phase diagram is shown in Fig. 3c of the main text.

To complement the ARPES data shown in Extended Data Fig. 3, we carried out more first-principles calculations on the BiSe/monolayer $NbSe_2$ heterostructure and found that it maintains a Fermi surface as large as that in monolayer $NbSe_2$. Here, the monolayer $NbSe_2$ accepts ~0.04*e* from the cubic BiSe layer and thus the band filling occupation of the monolayer $NbSe_2$ layer does not show significant change. The charge transfer between $\sqrt{2} \times 4\sqrt{2}$ BiSe on $\sqrt{3} \times 7$ $NbSe_2$ layers (Extended Data Fig. 8) is estimated from the vertical dipole moment and interlayer separation from our first-principles calculations. Based on the calculated ~1.5 *e*Å dipole moment for the entire supercell and a lower estimate of the interlayer separation ~2.7 Å (between the upper Se layer in monolayer $NbSe_2$ and lower Bi layer in BiSe), we found that the charge transfer per $NbSe_2$ formula unit is ~0.04*e*. This charge transfer is small because any small charge transfer between two layers sets up a vertical electric field between the layers that opposes further the charge transfer, similar to the case in a prior study [19]. The smallness of the charge transfer is also reflected in the Fermi level in monolayer $NbSe_2$ largely remaining at a level that half-fills its top valence band after the coverage of the BiSe layer, as shown in the projected band structures of BiSe/monolayer $NbSe_2$ (Extended Data Fig. 8b left) and freestanding monolayer $NbSe_2$ ((Extended Data Fig. 8b right).

In freestanding *m*QL Bi_2Se_3 films, (*m*–1) QW states are expected to appear in the bulk conduction bands, as highlighted in orange in the calculated band structures (Extended Data Fig. 9). In our ARPES experiments, we observed only the first two QW states for the $m \leq 6$ samples. We may resolve more bulk QW states in highly electron doped Bi_2Se_3 films with $m \geq 4$. Note that in our DFT calculations, we ignored the effect of the substrates and did not include any defects and disorders (e.g. Se vacancies) in the supercells of the *m*QL Bi_2Se_3. Therefore, the calculated band structures here do not include the information of the Dirac point shift in Bi_2Se_3 films with increasing *m* observed in our ARPES experiments (Fig. 2 and Extended Data Fig. 4).

In the main text, we associated the three QW states in the 3QL Bi_2Se_3/BiSe heterostructure to the three QW states in a 4QL Bi_2Se_3 film, due to the similarities in their partial charge densities (see Fig. 4g). To demonstrate the defining characteristics of the three QW states in a 4QL Bi_2Se_3 film, we plotted the partial charge densities of QW1, QW2, and QW3 using yellow isosurfaces, along with their *xy*-plane-averaged representations $\rho_{xy}(z)$ (Extended Data Fig.10). We also sketched out the charge densities of the envelope wavefunctions of these states in black curves. The three QW states can be identified by the number of nodes in their envelope wavefunctions: 0, 1, and 2 nodes for QW1, QW2, and QW3.

II. Supplementary Text for Supplementary Figs. 1 to 6.

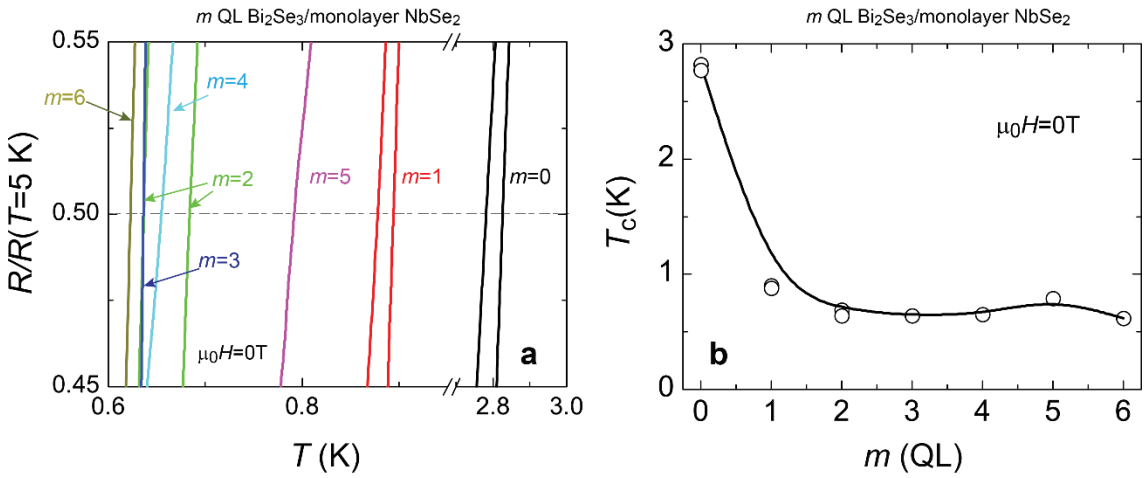

Supplementary Fig. 1| T_c of the m QL Bi_2Se_3/monolayer $NbSe_2$ heterostructures. (a) Enlarged R-T curves of the m QL Bi_2Se_3/monolayer $NbSe_2$ heterostructures under zero magnetic field. R is normalized to the normal state resistance at T =5 K. (b) T_c of the m QL Bi_2Se_3/monolayer $NbSe_2$ heterostructures as a function of m. T_c is determined by the temperature at which $R/R(T=5K) \sim 0.5$. Two m=0, m=1, and m=2 samples are included in (a and b).

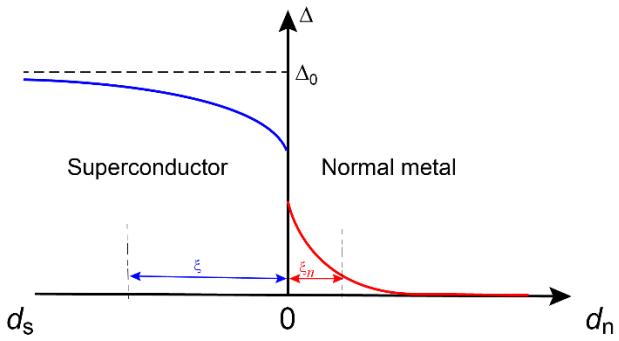

Supplementary Fig. 2| Superconducting proximity effect in normal metal/superconductor heterostructures. The superconducting pairing potential Δ near a normal metal/superconductor interface. Δ_0 is the pairing potential deep into a bulk superconductor. Two superconducting coherence lengths ξ_n and ξ are involved here.

Supplementary Fig. 1a shows the enlarged R-T curves of the m QL Bi_2Se_3/monolayer $NbSe_2$ heterostructures with $0 \leq m \leq 6$ under zero magnetic field (Fig. 3a of the main text). Supplementary Fig. S1b shows the T_c value of mQL Bi_2Se_3/monolayer $NbSe_2$ heterostructures as a function of m. Here, we found that the value of T_c decreases from ~2.8 K for the monolayer

$NbSe_2$ to ~0.6 K for the $m = 6$ sample. The superconducting proximity effect-induced T_c reduction in Bi_2Se_3/monolayer $NbSe_2$ heterostructures can be attributed to the "leakage" of Cooper pairs from the monolayer $NbSe_2$ into the Bi_2Se_3 layer. For a normal metal/superconductor interface, the superconducting pairing potential Δ as a function of depth is shown in Supplementary Fig. S2. On the normal metal side, the pairing potential is nonzero and decreases over a length scale ξ_n into the metal. On the superconductor side, the pairing potential decreases over a length scale ξ from its bulk value Δ_0 towards the interface. In other words, the thinner the superconductor used in normal metal/superconductor heterostructures, there should be a stronger T_c reduction with increasing thickness of the normal metal layer [20,21]. In our experiments, the superconductor is monolayer $NbSe_2$, which is much thinner than ξ ~2.3 nm of bulk $NbSe_2$ (Ref.[22]), the superconducting pairing potential Δ is greatly reduced in monolayer $NbSe_2$ when it is covered by Bi_2Se_3 films. Therefore, the value of T_c, which is determined by the pairing potential Δ of the monolayer $NbSe_2$, actually decreases with increasing the thickness of Bi_2Se_3 films.

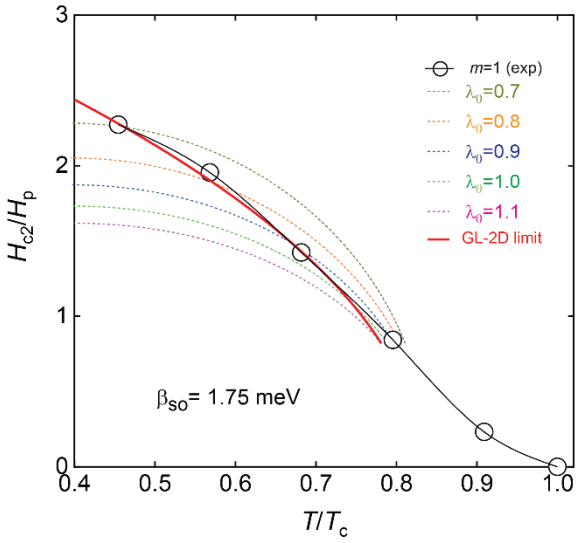

Supplementary Fig. 3 | Theoretical calculations of the 1QL Bi_2Se_3/monolayer $NbSe_2$ heterostructure. The calculated in-plane upper critical magnetic field normalized to the Pauli paramagnetic field $H_{c2,\parallel}/H_P$ as a function of the normalized temperature T/T_c under different inter-valley scattering λ_0 and β_{so}=1.75 meV. The experimental data of the $m = 1$ sample cannot be fitted by either linear-T behavior (GL-3D limit) or square-root-T behavior (GL-2D limit, red solid line). A moderate fit with λ_0~0.9 meV and β_{so}~1.75 meV suggests that the inter-valley scattering may provide an alternative explanation for the reduction of $H_{c2,\parallel}/H_P$ in 1 QL Bi_2Se_3/monolayer $NbSe_2$ heterostructure .

We now present an alternative understanding for the reduction of $H_{c2,\parallel}$ in the 1QL Bi_2Se_3/monolayer $NbSe_2$ heterostructure, compared to the $H_{c2,\parallel}$ value in monolayer $NbSe_2$. Our STEM measurements clearly show that a BiSe layer is stabilized between monolayer $NbSe_2$ and Bi_2Se_3 layers (Fig. 1b and Extended Data Fig. 2). Since this interfacial BiSe layer has a cubic lattice structure, it might induce a moiré potential to the bottom monolayer $NbSe_2$. Therefore, we phenomenologically introduced an inter-layer inter-valley scattering potential λ_0 to investigate the suppression of $H_{c2,\parallel}/H_P$ through tuning λ_0. In our calculations, we considered the following

model Hamiltonian without Rashba spin-orbit coupling for the 1QL Bi_2Se_3/monolayer $NbSe_2$ heterostructure,

$$H_0 = \left(\frac{p^2}{2m_h} - \mu\right)\tau_0 s_0 + \beta_{so}\tau_z s_z + H_x s_x + \lambda_0 \tau_x s_0 \quad \text{(S2)}$$

Here, we assumed λ_0 to be momentum independent. Using Eq. (S2), the solution of Eq. (7) in the Method section of the main text was given by

$$\mathrm{Log}\left[\frac{\mathrm{T}}{\mathrm{T_c}}\right] = \frac{1}{2}[C_0(\rho_-) + C_0(\rho_+)] + \frac{1}{2}[C_0(\rho_-) - C_0(\rho_+)] \times \frac{\beta_{so}^2 + \lambda_0^2 - H_x^2}{E_- E_+} \quad \text{(S3)}$$

where $\mathrm{E}_\pm = \sqrt{\beta_{so}^2 + (H_x \pm \lambda_0)^2}$ and $\rho_\pm = \frac{1}{2}(E_+ \pm E_-)$. Equation (S3) is mathematically equivalent to Eq. (8) for the Rashba case in the main text by replacing $\alpha_0 \rightarrow \lambda_0$. Therefore, we could similarly argue that a strong inter-valley scattering would lead to the suppression of $\mathrm{H}_{c2,\parallel}/H_P$ (Supplementary Fig. 3).

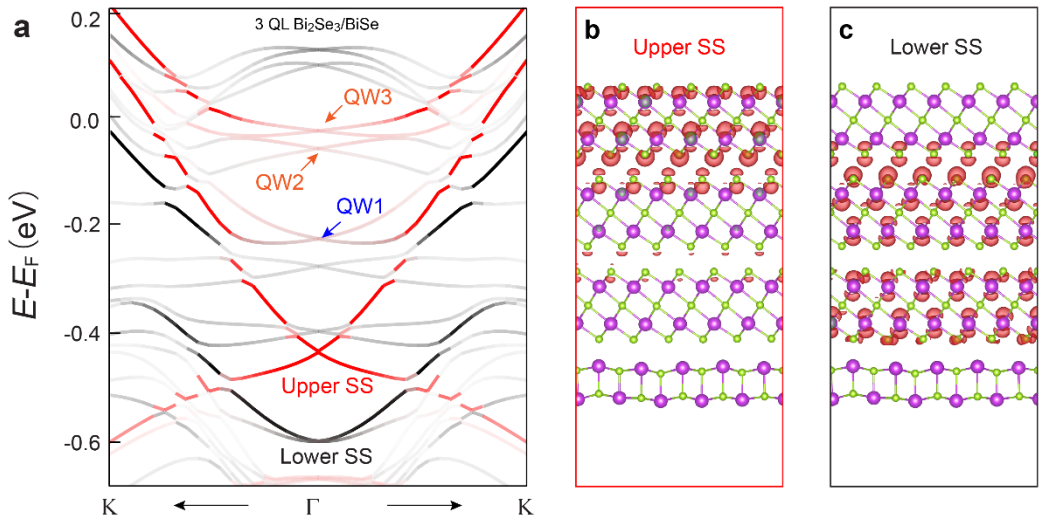

Supplenmentary Fig. 4 | Upper and lower Dirac SS in 3 QL Bi_2Se_3/BiSe heterostructure. (a) The calculated electronic band structure of 3QL Bi_2Se_3/BiSe. The projections of the total wave function onto Bi orbitals on the upper and lower surfaces of 3QL Bi_2Se_3 are shown in red and black. (b and c) Partial charge densities of upper SS (b) and lower SS (c). For comparison purposes, (a) and (b) are reused here from Figs. 4d and 4e in the main text.

In the main text, our first-principles calculations focus on the upper SS and the bulk QW bands in the 3QL Bi_2Se_3/BiSe system. Here we showed the lower SS (Supplementary Fig. 4c), represented by its partial charge density in red isosurfaces. The decay length of the lower SS into the 3QL Bi_2Se_3 interior (~2QL) is longer than that of the upper SS (~1QL). When the BiSe layer is removed, the decay length of the lower SS is found to be ~1 QL.

In Fig. 4d of the main text, the DFT calculated band structure of the 3 QL Bi_2Se_3/BiSe heterostructure shows a gap of ~17 meV for the upper SS near -0.5 eV (Supplementary Fig. 4a). The size of this small hybridization gap is comparable to the energy resolution of our ARPES analyzer at room temperature (~10 meV). Moreover, the structure used in our DFT calculations is a 3 QL Bi_2Se_3/BiSe bilayer rather than the real 3QL Bi_2Se_3/BiSe/monolayer $NbSe_2$ trilayer in our experiments. This may also introduce a small deviation between the DFT data and the ARPES

band map. Finally, we note that the absolute value of the calculated gap size is not intended to be quantitatively compared with the experimental data because the calculated gap size depends sensitively on the choice of the exchange-correlation functional or the overall theory level [23].

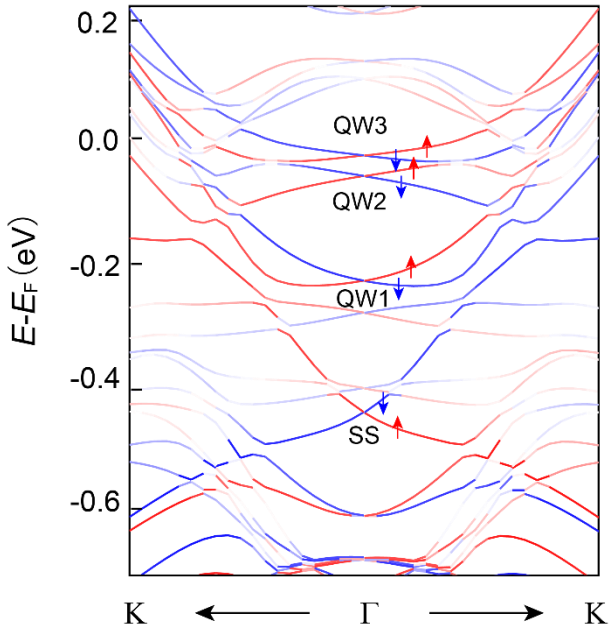

Supplenmentary Fig. 5 | Rashba-type spin textures in the 3QL Bi_2Se_3/BiSe heterostructure. Spin-projected band structure for the 3QL Bi_2Se_3/BiSe heterostructure. Γ-K sits along *x* and projections onto spins orienting along ±*y* are shown in red and blue, respectively.

We further calculated the spin textures of these three bulk QW bands (i.e. QW1, QW2, and QW3) and indeed found these three QW states show a Rashba-type spin texture (Supplementary Fig. 5). For states along *x* (i.e. Γ-K direction), spins are oriented along ±*y* as expected for Rashba-type spin splitting, with +*y* and –*y* orientations indicated by red and blue, respectively.

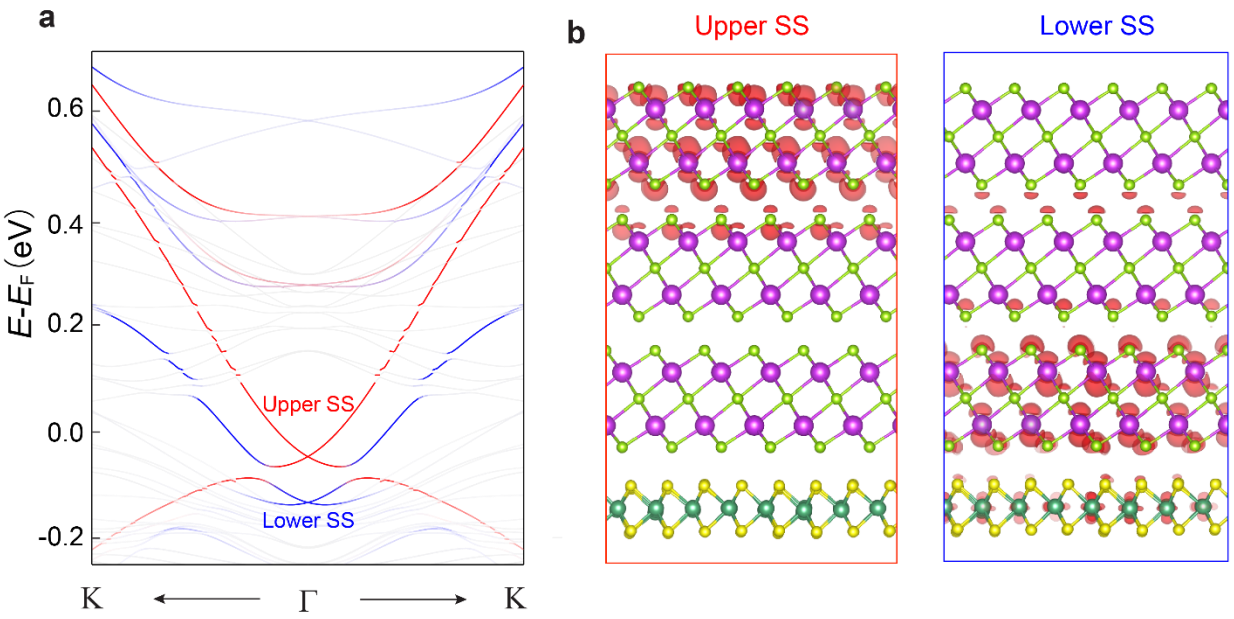

Supplenmentary Fig. 6 | First-principles calculations of 3 QL Bi_2Se_3/monolayer $NbSe_2$ without including the BiSe interfacial layer. (a) The calculated band structure of 3QL Bi_2Se_3/monolayer $NbSe_2$ heterostructure. The projections of the total wavefunction onto Bi orbitals on the upper and lower surfaces of 3QL Bi_2Se_3 are shown in red and blue, respectively. (b) Partial charge densities for the upper and lower SSs.

The large Rashba splitting of the *m*=3 sample in our ARPES data (E_R = 0.011eV, see Fig. 2) relies on QW states residing in an effective 4-layer structure (3QL Bi_2Se_3 + a bilayer BiSe) that has a built-in compositional asymmetry along *z*. The implicit condition for the above assumption is that the envelope wavefunction approximation is valid (i.e. the potential and wavefunctions vary slightly between 3QL Bi_2Se_3 and BiSe layers). This condition might be fulfilled by a BiSe bilayer because the BiSe bilayer and Bi_2Se_3 QL have the same elemental composition and are a part of the rocksalt lattice structure with a low-energy electronic structure determined by *p* orbital interactions[24].

If 3QL Bi_2Se_3 is grown on a substrate that is electronically distinct from Bi_2Se_3 QL, the weak interaction between Bi_2Se_3 and substrate can only slightly modulate the two QW states from 3QL

Bi_2Se_3 and thus these two QW states show a much smaller Rashba splitting. Supplementary Fig. 6a shows the projected band structure of 3QL Bi_2Se_3 on monolayer $NbSe_2$, without including the BiSe layer. Red and blue curves indicate the projection of the total wavefunction onto Bi orbitals in the uppermost and lowermost surface layers, respectively. The two-colored states below E-E_F =0eV can be identified to be a pristine upper SS (red) and a lower SS (blue). We found that the lower SS weakly hybridizes with $NbSe_2$ (the corresponding $NbSe_2$-majority and lower-SS-minority hybrid state is at E-E_F = +0.6eV). This is further confirmed by their real-space partial charge densities in Supplementary Fig. 6b. For +0.2eV ≤ (E-E_F) ≤ +0.4 eV, two QW states appear, as expected from 3QL Bi_2Se_3. Since these QW wavefunctions are confined within 3QL Bi_2Se_3, they do not interact strongly with the bottom monolayer $NbSe_2$. Therefore, the Rashba splitting of these QW states is only ~30% in magnitude compared with those in the 3QL Bi_2Se_3/BiSe heterostructure, as discussed in the main text.

References

1 Wang, M. X., Li, P., Xu, J. P., Liu, Z. L., Ge, J. F., Wang, G. Y., Yang, X. J., Xu, Z. A., Ji, S. H., Gao, C. L., Qian, D., Luo, W. D., Liu, C. H. & Jia, J. F. Interface structure of a topological insulator/superconductor heterostructure. *New J. Phys.* **16**, 123043 (2014).

2 Ugeda, M. M., Bradley, A. J., Zhang, Y., Onishi, S., Chen, Y., Ruan, W., Ojeda-Aristizabal, C., Ryu, H., Edmonds, M. T., Tsai, H. Z., Riss, A., Mo, S. K., Lee, D. H., Zettl, A., Hussain, Z., Shen, Z. X. & Crommie, M. F. Characterization of collective ground states in single-layer $NbSe_2$. *Nat. Phys.* **12**, 92-97 (2016).

3 Xu, C. Z., Wang, X. X., Chen, P., Flototto, D., Hlevyack, J. A., Lin, M. K., Bian, G., Mo, S. K. & Chiang, T. C. Experimental and theoretical electronic structure and symmetry effects in ultrathin $NbSe_2$ films. *Phys. Rev. Mater.* **2**, 064002 (2018).

4 Zhang, Y., He, K., Chang, C. Z., Song, C. L., Wang, L. L., Chen, X., Jia, J. F., Fang, Z., Dai, X., Shan, W. Y., Shen, S. Q., Niu, Q., Qi, X. L., Zhang, S. C., Ma, X. C. & Xue, Q. K. Crossover of the Three-Dimensional Topological Insulator Bi_2Se_3 to the Two-Dimensional Limit. *Nat. Phys.* **6**, 584-588 (2010).

5 Liu, C. X., Zhang, H., Yan, B. H., Qi, X. L., Frauenheim, T., Dai, X., Fang, Z. & Zhang, S. C. Oscillatory Crossover from Two-Dimensional to Three-Dimensional Topological Insulators. *Phys. Rev. B* **81**, 041307 (2010).

6 Michiardi, M., Bianchi, M., Dendzik, M., Miwa, J. A., Hoesch, M., Kim, T. K., Matzen, P., Mi, J. L., Bremholm, M., Iversen, B. B. & Hofmann, P. Strongly anisotropic spin-orbit splitting in a two-dimensional electron gas. *Phys. Rev. B* **91**, 035445 (2015).

7 Zhu, Z. H., Levy, G., Ludbrook, B., Veenstra, C. N., Rosen, J. A., Comin, R., Wong, D., Dosanjh, P., Ubaldini, A., Syers, P., Butch, N. P., Paglione, J., Elfimov, I. S. & Damascelli, A. Rashba Spin-Splitting Control at the Surface of the Topological Insulator Bi_2Se_3. *Phys. Rev. Lett.* **107**, 186405 (2011).

8 Valla, T., Pan, Z. H., Gardner, D., Lee, Y. S. & Chu, S. Photoemission Spectroscopy of Magnetic and Nonmagnetic Impurities on the Surface of the Bi_2Se_3 Topological Insulator. *Phys. Rev. Lett.* **108**, 117601 (2012).

9 King, P. D. C., Hatch, R. C., Bianchi, M., Ovsyannikov, R., Lupulescu, C., Landolt, G., Slomski, B., Dil, J. H., Guan, D., Mi, J. L., Rienks, E. D. L., Fink, J., Lindblad, A.,

Svensson, S., Bao, S., Balakrishnan, G., Iversen, B. B., Osterwalder, J., Eberhardt, W., Baumberger, F. & Hofmann, P. Large Tunable Rashba Spin Splitting of a Two-Dimensional Electron Gas in Bi_2Se_3. *Phys. Rev. Lett.* **107**, 096802 (2011).

10 Bahramy, M. S., King, P. D. C., de la Torre, A., Chang, J., Shi, M., Patthey, L., Balakrishnan, G., Hofmann, P., Arita, R., Nagaosa, N. & Baumberger, F. Emergent quantum confinement at topological insulator surfaces. *Nat. Commun.* **3**, 1159 (2012).

11 Nitta, J., Akazaki, T., Takayanagi, H. & Enoki, T. Gate control of spin-orbit interaction in an inverted $In_{0.53}Ga_{0.47}As/In_{0.52}Al_{0.48}$ as heterostructure. *Phys. Rev. Lett.* **78**, 1335-1338 (1997).

12 Luo, J., Munekata, H., Fang, F. & Stiles, P. Effects of inversion asymmetry on electron energy band structures in GaSb/InAs/GaSb quantum wells. *Phys. Rev. B* **41**, 7685 (1990).

13 Das, B., Miller, D., Datta, S., Reifenberger, R., Hong, W., Bhattacharya, P., Singh, J. & Jaffe, M. Evidence for spin splitting in $In_xGa_{1-x}As/In_{0.52}Al_{0.48}As$ heterostructures as $B \rightarrow 0$. *Phys. Rev. B* **39**, 1411 (1989).

14 Chang, C. Z., He, K., Wang, L. L., Ma, X. C., Liu, M. H., Zhang, Z. C., Chen, X., Wang, Y. Y. & Xue, Q. K. Growth of Quantum Well Films of Topological Insulator Bi_2Se_3 on Insulating Substrate. *SPIN* **1**, 21-25 (2011).

15 Sakamoto, Y., Hirahara, T., Miyazaki, H., Kimura, S. & Hasegawa, S. Spectroscopic evidence of a topological quantum phase transition in ultrathin Bi_2Se_3 films. *Phys. Rev. B* **81**, 165432 (2010).

16 Xia, Y., Qian, D., Hsieh, D., Wray, L., Pal, A., Lin, H., Bansil, A., Grauer, D., Hor, Y. S., Cava, R. J. & Hasan, M. Z. Observation of a Large-Gap Topological-Insulator Class with a Single Dirac Cone on the Surface. *Nat. Phys.* **5**, 398-402 (2009).

17 Xi, X. X., Wang, Z. F., Zhao, W. W., Park, J. H., Law, K. T., Berger, H., Forro, L., Shan, J. & Mak, K. F. Ising pairing in superconducting $NbSe_2$ atomic layers. *Nat. Phys.* **12**, 139-143 (2016).

18 Xing, Y., Zhao, R., Shan, P. J., Zheng, F. P., Zhang, Y. W., Fu, H. L., Liu, Y., Tian, M. L., Xi, C. Y., Liu, H. W., Feng, J., Lin, X., Ji, S. H., Chen, X., Xue, Q. K. & Wang, J. Ising Superconductivity and Quantum Phase Transition in Macro-Size Monolayer $NbSe_2$. *Nano Lett.* **17**, 6802-6807 (2017).

19 Khomyakov, P. A., Giovannetti, G., Rusu, P. C., Brocks, G., van den Brink, J. & Kelly, P. J. First-principles study of the interaction and charge transfer between graphene and metals. *Phys. Rev. B* **79**, 195425 (2009).

20 Stellhorn, A. *Interplay of Proximity Effects in Superconductor/ferromagnet Heterostructures*. Vol. 242 (Forschungszentrum Jülich GmbH, 2021).

21 Buzdin, A. I. Proximity effects in superconductor-ferromagnet heterostructures. *Rev. Mod. Phys.* **77**, 935-976 (2005).

22 Tessmer, S. H., Tarlie, M. B., VanHarlingen, D. J., Maslov, D. L. & Goldbart, P. M. Probing the superconducting proximity effect in $NbSe_2$ by scanning tunneling microscopy. *Phys. Rev. Lett.* **77**, 924-927 (1996).

23 Reid, T. K., Alpay, S. P., Balatsky, A. V. & Nayak, S. K. First-principles modeling of binary layered topological insulators: Structural optimization and exchange-correlation functionals. *Phys. Rev. B* **101**, 085140 (2020).

24 Lind, H., Lidin, S. & Haussermann, U. Structure and bonding properties of $(Bi_2Se_3)_m(Bi_2)_n$ stacks by first-principles density functional theory. *Phys. Rev. B* **72**, 184101 (2005).